



Nanostructuring of an additively manufactured CoCrFeNi multi-principal element alloy using severe plastic deformation: Comparison of two materials processed by different laser scan speeds

Kamilla Mukhtarova^a, Megumi Kawasaki^b, Zoltán Dankházi^a, Márk Windisch^{a,c}, György Zoltán Radnóczy^d, Weronika Serafimowicz^e, Jenő Gubicza^{a,*}

^a Department of Materials Physics, Eötvös Loránd University, P.O.B. 32, H-1518, Budapest, Hungary

^b School of Mechanical, Industrial and Manufacturing Engineering, Oregon State University, Corvallis, 97331, OR, USA

^c Department of Development, Bay Zoltán Nonprofit Ltd. for Applied Research, H-1116, Budapest, Hungary

^d Institute for Technical Physics and Materials Science, Centre for Energy Research, Konkoly-Thege M. út 29-33., H-1121, Budapest, Hungary

^e Technoorg Linda Co. Ltd, H-1044, Budapest, Hungary

ARTICLE INFO

Keywords:

- A. high-entropy alloys
- A. nanocrystalline metals
- B. mechanical properties
- C. severe plastic deformation
- D. microstructure
- F. diffraction/scattering

ABSTRACT

Experiments were conducted to reveal the refinement of the microstructure and the evolution of the hardness of an additively manufactured (AM) CoCrFeNi multi-principal element alloy (MPEA) processed by severe plastic deformation (SPD) using high pressure torsion (HPT) technique. AM was carried out by laser powder bed fusion (L-PBF) technique at two different laser scan speeds. The as-built alloys for both laser scan speeds have a single-phase face-centered cubic (fcc) structure with $\langle 110 \rangle$ fiber texture parallel to the building direction. X-ray line profile analysis (XLPA) revealed that the dislocation density was considerably high even in the AM-processed state before HPT ($3 \times 10^{14} \text{ m}^{-2}$) which increased by two orders of magnitude during HPT. The saturation of the lattice defects (dislocation density and twin fault probability) as well as the crystallite size occurred at a shear strain of about 10 during HPT. In both AM-processed alloys, $\langle 111 \rangle$ fiber texture developed parallel to the normal of the HPT-processed disks. For both laser scan speeds, the initial grain size in the AM-processed samples was refined from 70 to 90 μm to the nanocrystalline regime after 10 turns of HPT. Additionally, nanotwins formed with a probability of about 3 %. The initial hardness of the AM-processed MPEA samples for both laser scan speeds was 2700–2800 MPa, which is superior to that of CoCrFeNi produced by casting (about 1380 MPa). This can be explained by the high dislocation density in the AM-processed specimens. The formation of nanostructure with high lattice defect density during HPT resulted in a very high hardness value of about 5500 MPa in the AM-processed CoCrFeNi MPEA samples for both laser scan speeds.

1. Introduction

Multi-Principal Element Alloys (MPEAs), also known as Complex Concentrated Alloys (CCAs), are a new class of materials composed of three or more principal elements in equal or near-equal atomic proportions [1,2]. If MPEAs contain at least five elements, the high configuration entropy tends to stabilize a single solid-solution with several kinds of crystal structures such as face-centered cubic (FCC), body-centered cubic (BCC) and hexagonal close-packed (HCP) phases [3]. This type of alloy has attracted widespread interest due to its excellent performance such as the combination of high strength and good ductility in a wide range of temperatures [4–7], excellent

resistance to wear [8,9], corrosion [10,11] and fatigue [12], good thermal stability [13,14]. Potential applications of MPEAs include high-temperature turbine blades [15], molds and dies, hard coatings for cutting tools [16], catalysts [17,18], bone scaffolds, plates [19] and coatings for orthopedic implants [20].

MPEAs are typically produced by vacuum arc melting and powder metallurgy [21–24]. Production by arc melting requires extensive remelting and ingot inverting; furthermore, there are some disadvantages such as composition segregation, defects and large inner stress [25]. Powder metallurgy consists of several steps: powder production, powder mixing and consolidation. After that, the fabricated sample is subjected to various operations such as rolling, extrusion and annealing

* Corresponding author.

E-mail address: jeno.gubicza@ttk.elte.hu (J. Gubicza).

<https://doi.org/10.1016/j.intermet.2024.108336>

Received 15 February 2024; Received in revised form 6 May 2024; Accepted 20 May 2024

Available online 24 May 2024

0966-9795/© 2024 The Authors. Published by Elsevier Ltd. This is an open access article under the CC BY license (<http://creativecommons.org/licenses/by/4.0/>).

in order to achieve an improved microstructure [26]. Powders for sintering can be produced by atomization and mechanical alloying. The weakness of mechanical alloying is the possible contamination of the powder from the grinding media. Consolidation is usually proceeded by spark plasma sintering (SPS), other methods such as hot pressing (HP) or hot isostatic pressing (HIP) can also be used. However, these methods usually require higher temperatures and longer times compared to SPS, so grain growth is not fully avoided [23]. Many constraints on shape and scale need to be considered when using these techniques.

In contrast, additive manufacturing (AM) enables the production of complex geometries with less consuming time [27–30]. AM route, also known as 3D printing, is a technology in which the part is built up layer by layer according to computer aided design (CAD) data [31,32]. A wide range of materials, including metals, polymers, and ceramics, can be used to produce components [33,34]. In addition, AM offers several benefits, such as reduced material waste [27,31], rapid prototyping [28,29], cost savings for small production runs [27,35], environmental friendliness [36], and supply chain flexibility [37,38]. AM has a wide range of applications across various industries, including aerospace [39–41], medical [42–44], and automotive [45,46].

Among AM techniques, specified by ASTM 52900 guidelines [47], the most frequently applied method for processing metals and alloys is the powder bed fusion (PBF). This method utilizes a high-energy power source, such as a laser or an electron beam, to selectively melt a metallic powder bed [48]. In the first step of laser powder bed fusion (L-PBF), the layer of metal powder is spread onto the building platform, then the laser beam selectively melts the desired area. In the last step, the building platform is lowered down and a new layer of powder is spread. This process is repeated until the final part is formed. Due to the complexity of the L-PBF process, there are many different processing parameters, but the most important ones are the laser power, the layer thickness, the laser scan velocity, the hatch distance (distance between successive laser passes) and the scanning strategy (laser scanning pattern on each layer) [49].

L-PBF process results in a microstructure that differs from its as-cast counterparts. These differences arise from various factors, such as the high cooling rate, the high temperature of the melt pool, the steep temperature gradients, and thermal cycling during manufacturing. During L-PBF processing, the material is epitaxially nucleated on the underlying layer. Epitaxy refers to the oriented growth of one crystal on the surface of another crystal. This process results in newly growing cells/dendrites having the same crystallographic orientation as grains in the substrate or previously solidified layers [50]. The solidification mode is determined by the ratio of temperature gradient (G) to growth rate (R), while their product determines the feature size (e.g., grain size) of the as-received microstructures. The solidification microstructures can be planar, cellular, columnar, or equiaxed dendritic with decreasing G/R ratio values. The most widely observed microstructures are columnar and equiaxed [51]. For instance, 316 L and Inconel 718 alloys manufactured by selective laser melting (SLM) solidified in the cellular-dendritic regime while in Ti-6Al-4V columnar microstructure was observed [52–55]. Submicron cells of dislocations were also observed in the post-solidification microstructure. Thermal stresses generated by the cyclic expansion and contraction of different layers during additive manufacturing stimulate the clustering of dislocation cells, thus, providing an additional strengthening effect to the material compared with those fabricated by traditional methods [56–58].

Rapid solidification and strong thermal gradients in the melt pool result in a textured microstructure in the AM-processed materials. The preferential growth direction for cubic structures is $\langle 100 \rangle$ direction since the heat transfer from the growing crystal to the liquid phase in the melt pool is the highest in this direction [33,49,59]. For instance, the common texture in Inconel 718 alloy is $\langle 100 \rangle$. On the other hand, it is possible to change the texture by varying the laser scan speed. For example, in Inconel 718 alloy a single-crystal-like microstructure with $\langle 110 \rangle$ orientation in the building direction (BD) developed at the laser

scan speeds of 1400 mm/s. When the laser speed decreased to 1000 mm/s, a second texture component with $\langle 100 \rangle$ orientation parallel to the BD formed [60]. In SLM-processed 316 L steel, single component $\langle 100 \rangle$ texture, two-component textures comprising of $\langle 110 \rangle$ and $\langle 100 \rangle$ orientations, and a random texture were produced by varying the laser scan speed [61].

The first research on the production of MPEAs by AM was conducted in 2013 when a ZrTiVCrFeNi high entropy alloy (HEA) was successfully produced using Laser Engineered Net Shaping (LENS) [62]. The processing of MPEAs by AM has been studied extensively; for instance, an equiatomic FeCoCrNi HEA was manufactured by SLM and it showed a combination of high strength and good ductility [63]. It was also found that an $Al_{0.3}CoCrFeNiCu$ HEA produced by SLM exhibited superior mechanical properties compared to its as-cast counterpart [64]. Zhao et al. fabricated a stepwise compositionally graded $CoCrFeNiTi_x$ ($x = 0-0.6$) HEA and revealed that a maximum of ~ 10 at.% Ti addition led to a higher hardness [65]. An equiatomic $CoCrFeNi$ HEA with B_4C reinforcing particles was produced by the L-PBF technique and showed much higher tensile yield and ultimate strength values (1250 MPa and 1421 MPa, respectively) compared to $CoCrFeNi$ (625 MPa and 691 MPa, respectively) at room temperature (RT) [66]. It should be noted that AM techniques can also be used for producing combinatorial MPEAs in which the concentration of one or more constituents varies in a single sample [67]. The application of combinatorial samples can facilitate finding the optimal composition of MPEAs for a desired performance.

The behavior of AM-processed MPEAs at very high strains (higher than 100 %) can be tested using severe plastic deformation (SPD) techniques [68]. These methods apply high hydrostatic stress to suppress cracking during deformation for refining microstructure, thereby achieving extremely large strains without failure of the specimen. Among the SPD methods, high pressure torsion (HPT) yields the highest equivalent strain, ranging even up to 50,000 % [69–73]. The motivation of this study is to reveal the significance of such severe straining leading to severe microstructural refinement on the AM-processed $CoCrFeNi$ alloy. In order to achieve this goal, the microstructure and microhardness of AM-processed $CoCrFeNi$ MPEA with two different laser scan speeds were investigated after different amounts of HPT straining. Although the influence of SPD on the $CoCrFeNi$ MPEA family (e.g., on the $CoCrFeNiMn$ Cantor alloy) has been extensively studied [74–78], the SPD-induced changes on the AM-induced microstructure and mechanical behavior have only been rarely investigated [79]. Electron backscatter diffraction (EBSD) and transmission electron microscopy (TEM) were used to study the microstructure of the AM-processed samples before and after HPT-processing, respectively. X-ray line profile analysis (XLP), which is a non-destructive and effective method, was used to investigate the crystallite size and density of lattice defects (e.g. dislocations and twin faults) in the as-built and the HPT-processed samples. In addition, the change in hardness and crystallographic texture during HPT was monitored. The microstructure and hardness of the AM-processed alloy were also compared with an as-cast counterpart.

2. Materials and methods

2.1. AM processing of $CoCrFeNi$ MPEA

Bulk specimens were manufactured from a $Co_{25}Cr_{25}Fe_{25}Ni_{25}$ powder with a mean particle size of $37 \pm 17 \mu m$. The AM-processing of the bulk samples was conducted by L-PBF using a TruPrint 1000 3D printer (manufacturer: TRUMPF, Ditzingen, Germany). During the printing procedure, the Chess X–Y scan strategy was applied, i.e., the as-printed sample contained a chessboard structure. This means that square patterns with sides of 4 mm were reprinted by 90° -rotated printing directions and each consecutive layer shifts the pattern by 2.7577 and 3.2527 mm along the X- and Y-axis, respectively. Samples were printed at two laser scan speeds: 500 and 700 mm/s denoted as LS1 and LS2, respectively, with the same laser power of 150 W. The laser spot

diameter and the layer thickness were 55 μm and 20 μm , respectively. The value of hatch spacing was set as 80 μm . The printing process was performed in an Ar atmosphere with a gas flow velocity of 2.5 m/s. The oxygen concentration in the 3D printing device was less than 0.3 at. %.

2.2. HPT processing of the 3D-printed CoCrFeNi MPEA

The as-built samples were printed in the form of bars with a length of 65 mm and a diameter of 12 mm, and cut into disks with a cross-section diameter of 10 mm and thickness of ~ 0.85 mm. Processing by HPT was conducted by utilizing a conventional HPT facility with a quasi-constrained set-up [80]. The surface of the HPT disks was perpendicular to the AM building direction. The processing was operated at RT under 6.0 GPa at the rotational speed of 1 rpm for $\frac{1}{2}$, 1, 5 and 10 turns. The thickness of the disks was about 0.7 mm after HPT for all numbers of turns.

2.3. Microstructure study performed by electron microscopy

The AM-processed samples were examined by electron backscatter diffraction (EBSD) using a JEOL IT700HR-LA field emission scanning electron microscope (SEM) equipped with an Oxford Symmetry S3 EBSD detector. This study was performed on the plane lying perpendicular to the building direction. The accelerating voltage of the electron beam and the step size were 20 kV and 0.5 μm , respectively. The measured data was evaluated using Oxford AztecCrystal software and the datasets were filtered by routine cleaning process (wild spike and iterative zero solution process) in the AztecCrystal software. The grain size was determined by considering high-angle grain boundaries (misorientation angle greater than 15°) and areas of at least 10 pixels on the evaluated inverse pole Fig. s (IPF). Energy dispersive X-ray spectroscopy (EDS) was used to determine the chemical composition of the specimens. The surfaces of the samples for the SEM study were first mechanically polished with 1200, 2500 and 4000 grit SiC abrasive papers, and then the polishing was continued with a colloidal alumina suspension with a particle size of 1 μm and then 0.5 μm . In the final step of mechanical polishing, the samples were polished with a colloidal silica suspension (OP-S) with a particle size of 40 nm. Finally, the surfaces were electropolished at 25 V and 1 A with Struers A3 electrolyte.

The microstructure of the samples HPT-processed up to the highest number of turns (10) at the disk edge was investigated by transmission electron microscopy (TEM). Thin sections were cut at about 1 mm distance from the disk edge, perpendicular to the radius and the circular surface of the disk by a dual beam FIB/SEM instrument Scios II (manufacturer: Thermo Fisher Scientific, Waltham, MA, USA) using a focused Ga^+ beam. For cutting and polishing 30 kV and 5 kV accelerating voltages were used respectively. After the FIB process, a Technoorg Linda LEGtoSEM prototype instrument (similar to Technoorg's Gentle-Mill in cleaning effect) was used to clean the sample surface with a broad Ar^+ ion beam with accelerating voltages of 500 V and 300 V. This process results in a very clean surface enabling imaging of fine details in very thin parts of the sample such as nano-twin lamellae inside grains of about 50 nm size. A sample thickness less than the grain size is achieved on a limited area using a wedge shape section to avoid overlapping of different grains for optimum imaging. This rather small thickness implies the constraint for practically zero damaged surface layer (with a thickness less than 1–2 nm), which is reached by low energy Ar^+ ion milling. The cleaned thin sections were studied by a Themis 200 kV image-corrected transmission electron microscope with a nominal point resolution of 80 p.m. (manufacturer: Thermo Fisher Scientific, Waltham, MA, USA). Images showing nano-twin lamellae were recorded in high-resolution TEM (HRTEM) mode (without any objective aperture), while the search for these objects was done in bright field (BF) mode. Twin boundaries were imaged inside the grains which had their $\langle 110 \rangle$ type directions nearly parallel with the electron beam. In this orientation, the (111) plane of the twin boundary and the intersecting $\{111\}$

planes can be resolved to clearly prove the presence of twin boundary. During imaging no structural changes were observed in the samples due to beam damage or heating, i.e., the specimens were stable under the electron beam even at high magnifications with concentrated illumination. The grain sizes were determined from dark-field (DF) images since in these pictures the orientation differences can be seen better than in the BF micrographs.

2.4. Phase and texture analysis by X-ray diffraction

The phase composition of the AM-processed and the HPT-deformed CoCrFeNi samples was studied by XRD using a Smartlab powder diffractometer (manufacturer: Rigaku, Tokyo, Japan) with Bragg–Brentano geometry and a D/Tex Ultra 250 one dimensional detector. The diffractograms were measured on the surface lying perpendicular to the AM building direction using $\text{CuK}\alpha$ X-ray radiation with a wavelength of $\lambda = 0.15418$ nm in the 2θ range between 40° and 120° . The step size in 2θ was 0.01° . The diffractograms were evaluated with the PDXL2 program (manufacturer: Rigaku, Tokyo, Japan) using the ICDD-2018 database. The average lattice constant was determined from the diffraction peak positions using the Nelson-Riley method [81]. The crystallographic texture was measured by the same XRD machine. The texture was characterized by $\langle 111 \rangle$, $\langle 200 \rangle$ and $\langle 220 \rangle$ pole Fig. s (PFs) measured with parallel-beam optics. 3D-Explore software (manufacturer: Rigaku, Tokyo, Japan) was utilized to plot PFs. The sample surface before XRD experiments was prepared in the same way as for the EBSD study.

2.5. Characterization of the microstructure by XLPA

XLPA was applied to characterize the microstructure of the AM-processed samples and the HPT-deformed disks at the center and the edge. The surface preparation was the same as for the EBSD study (described in section 2.3). This analysis was carried out on diffractograms measured by high resolution diffractometer operating at 30 kV and 25 mA with $\text{CoK}\alpha_1$ radiation (wavelength: $\lambda = 0.1789$ nm) with a single crystal Ge monochromator. The spot size of the parallel X-ray beam on the surface of the samples was 0.2×2 mm². The scattered X-ray radiation was detected by two-dimensional imaging plates. The intensity at a given scattering angle (2θ) was obtained by integrating the signal along the corresponding Debye-Scherrer ring. The 2θ range between 40° and 120° with a step size of 0.014° was measured and evaluated. The X-ray diffraction peak profiles were evaluated by the Convolutional Multiple Whole Profile (CMWP) fitting method [82]. In this procedure, all measured diffraction peaks were fitted by the sum of a background spline and the convolution of theoretical microstructural profiles related to crystallite size, dislocation density and twin faults. In the CMWP fitting method, the crystallites are modelled by spheres with log-normal size distribution. The CMWP analysis provides the median (m) and the lognormal variance (σ^2) of the crystallite size distribution, the dislocation density and the twin fault probability. The twin fault probability for fcc materials gives the fraction of $\{111\}$ planes containing twin faults in percentage [83]. The area-weighted mean crystallite size was determined from m and σ^2 as $\langle x \rangle_{\text{area}} = m \cdot \exp(2.5 \sigma^2)$.

2.6. Determination of the porosity

The porosity in the AM-processed samples and the disks deformed for the highest number of turns ($N = 10$) was determined from the density measured with a pycnometer using distilled water. For obtaining the relative density, the measured density was divided with the theoretical density of the $\text{Co}_{25}\text{Cr}_{25}\text{Fe}_{25}\text{Ni}_{25}$ alloy which was calculated from the atomic mass values of the constituent elements and unit cell volume. The latter one was obtained from the lattice constant determined by X-ray diffraction (XRD). Thus, the following value of the theoretical density was used in the calculation of the relative density: 8.1804 g/cm³.

2.7. Hardness test

The hardness of the as-built and the HPT-processed samples was inspected using a Zwick Roell ZH μ indenter (manufacturer: ZwickRoell LP, Kennesaw, GA, USA) with an applied load of 500 g and a dwell time of 10 s. The spacing between the neighboring indents was 0.5 mm. The experiments were performed at RT. The as-built samples were indented ten times and then the mean of the hardness values was calculated. For the HPT-processed samples, the hardness was determined along the diameters of the disks.

3. Results

3.1. Microstructure and crystallographic texture of the AM-processed samples

Fig. 1 shows the XRD patterns of the as-built LS1 and LS2 samples. The XRD experiments revealed that both specimens have a full face-centered cubic (fcc) structure with a lattice parameter of 0.3577 ± 0.0002 nm. In addition, the high relative intensity of reflection 220 in the as-built LS1 sample indicates the development of a strong crystallographic texture. Therefore, $\langle 111 \rangle$, $\langle 200 \rangle$ and $\langle 220 \rangle$ PFs were measured by XRD which are shown in Fig. 2. The pole figures confirm $\langle 110 \rangle$ fiber texture for the as-built LS1 sample while the as-built LS2 sample has a less pronounced texture.

Table 1 lists the concentrations of the four elements in the as-built LS1, and LS2 samples as determined by SEM-EDS analysis. The results do not reveal any considerable difference between the chemical composition of the specimens AM-processed at two different laser scan speeds. For both samples, the composition is nearly equimolar, however, the atomic concentration of Cr is slightly below 25 % while for the other three constituents it is somewhat above that.

The EBSD images in Fig. 3a–c show the hierarchical microstructure of the as-built CoCrFeNi alloy for both LS1 and LS2 samples. The grain boundaries are indicated by black lines in the IPF maps. It is evident that the grains consist of columnar and equiaxed subgrains. The Kernel Average Misorientation (KAM) maps reveal highly distorted parts of the microstructure, which are related to low angle grain boundaries and represented by green color in Fig. 2b and d. The as-built LS1 and LS2 samples have an area-weighted mean grain size of 92 μm and 66 μm , respectively.

The crystallite size, the dislocation density and the twin fault probability in the as-built LS1 and LS2 samples as well as after HPT were determined by XLP. As an example, the CMWP fitting on the XRD pattern taken at the edge of the disk processed by HPT for 5 turns is shown in Fig. 4. The small values of the difference between the measured and calculated diffractograms indicate a good quality of fitting. No significant difference between the microstructural

parameters of the as-built samples LS1 and LS2 processed by the two laser scan speeds: the crystallite size and the dislocation density were around 300 nm and $3 \times 10^{14} \text{ m}^{-2}$, respectively, for both specimens. The twin fault probability was below the detection limit (0.1 %), i.e., the average twin fault spacing was at least 200 nm.

3.2. Microstructure evolution during HPT processing

The evolution of the crystallite size, dislocation density and twin fault probability of additively manufactured CoCrFeNi MPEA samples under different processing stages as a function of the nominal shear strain imposed during HPT is shown in Figs. 5–7, respectively. The value of γ was obtained as $\gamma = 2\pi rN/h$, where r is the distance from the disk center, N is the number of turns and h is the thickness of the disk [83]. Due to the extended height of the beam (2 mm, see section 2.5), the XRD pattern taken in the center corresponds to the distance from the center of $r = 0.5$ mm. Regarding the XLP study at the disk edge, due to the extended X-ray beam size the diffractogram was taken at a distance of 1 mm from the periphery, i.e., at $r = 4$ mm. In this study the lowest and the highest shear strain values were 2.2 and 360, respectively. These values are characteristic at the disk center for $\frac{1}{2}$ turn and edge for 10 turns.

The crystallite size decreased while the dislocation density and twin fault probability increased with increasing the shear strain for both samples LS1 and LS2 as shown in Figs. 5–7. The crystallite sizes of samples LS1 and LS2 were saturated with a consistent value of ~ 40 nm at the shear strain of about 20 as shown in Fig. 5a and b. The different laser scan speeds had no considerable effect on the saturation values of the crystallite size. Regarding the dislocation density, the saturation value of $\sim 300 \times 10^{14} \text{ m}^{-2}$ was achieved at the same shear strain of about $\gamma = 20$ for both samples LS1 and LS2. It should be noted, however, that the dislocation density increased slightly faster for sample LS2 at the shear strains lower than ~ 20 and saturated with a slightly higher value compared to specimen LS1 as indicated in the insets of Fig. 6a and b.

Fig. 7 shows that the twin fault probability for sample LS1 was saturated with the value of about 2.5 % at the shear strain of ~ 40 while for specimen LS2 the saturation occurred earlier (at $\gamma = 20$) with a slightly higher value of about 3 %. The slight difference between the evolution of the dislocation density and the twin fault probability for specimens LS1 and LS2 is discussed in section 4.

Fig. 8 shows BF and DF TEM images for the edge parts of the disks LS1 and LS2 processed by 10 turns of HPT. The grains in both samples are elongated. The grain length of specimens LS1 and LS2 is about 50–300 nm while the thickness ranges from about 10 to 50 nm. It can be seen that the grains in the DF-TEM images consist of subgrains with an average size of about 40 nm for both samples LS1 and LS2 which agrees well with the saturation crystallite size obtained by XLP.

The significance of twinning in the HPT-processed CoCrFeNi alloy

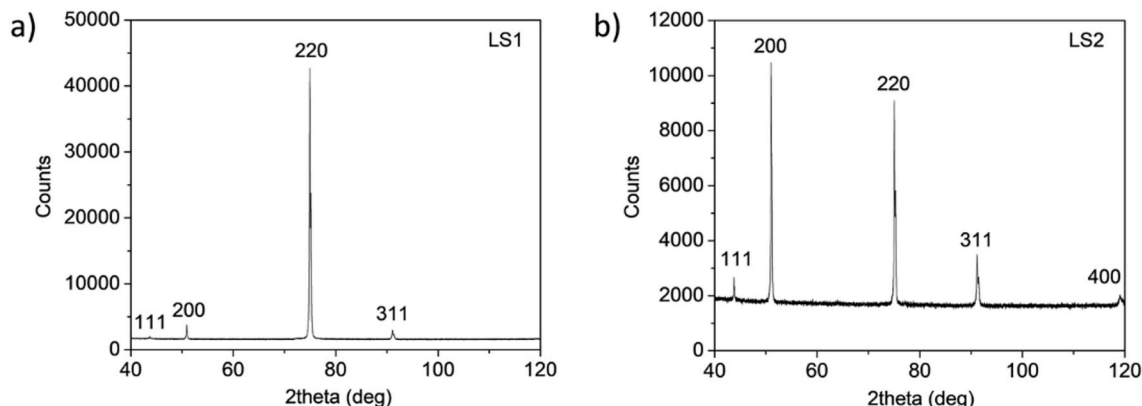


Fig. 1. XRD patterns taken on the as-built LS1 (a) and LS2 (b) CoCrFeNi samples.

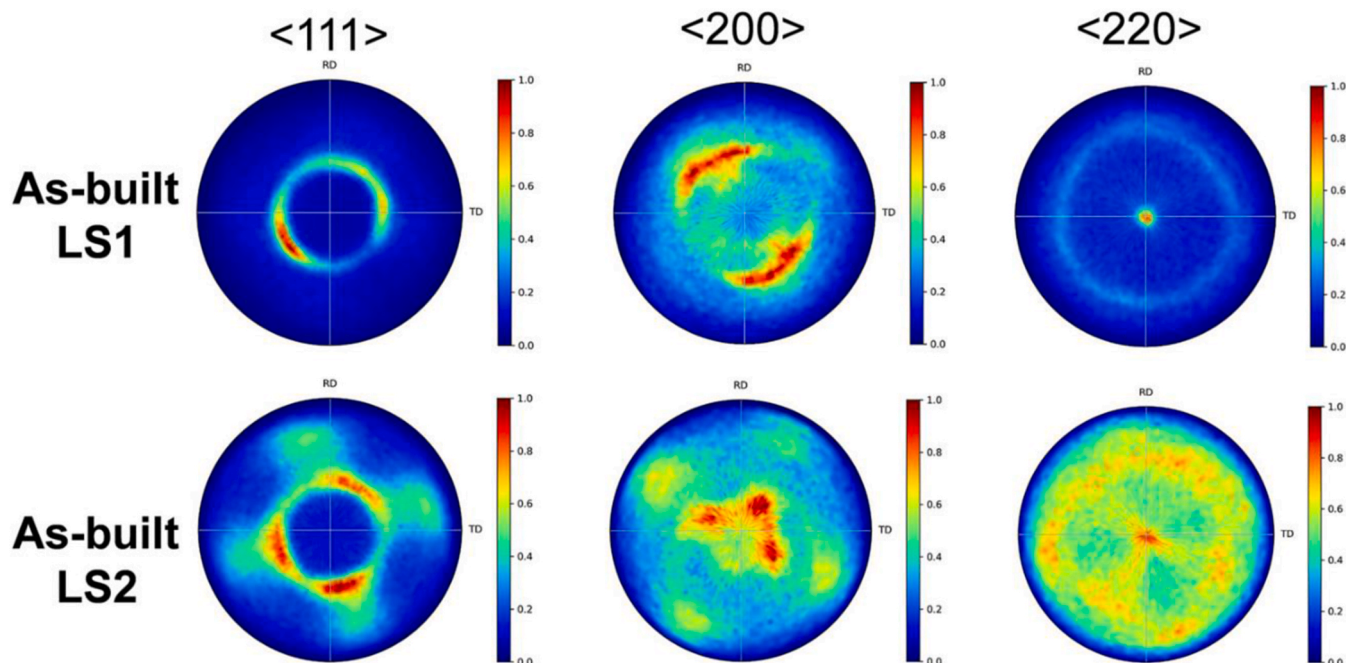


Fig. 2. $\langle 111 \rangle$, $\langle 200 \rangle$ and $\langle 220 \rangle$ XRD pole Fig. s obtained on the as-built LS1 and LS2 CoCrFeNi samples. The intensity in all pole Fig. s varies between zero and one due to normalization of the X-ray signal.

Table 1

Concentration of elements in the AM-processed LS1 and LS2 CoCrFeNi samples, and an as-cast specimen as measured by SEM-EDS.

Sample	Co [at.%]	Cr [at.%]	Fe [at.%]	Ni [at.%]
AM-processed, LS1	25.1 ± 0.1	24.1 ± 0.1	25.4 ± 0.1	25.4 ± 0.1
AM-processed, LS2	25.4 ± 0.1	23.7 ± 0.1	25.3 ± 0.1	25.6 ± 0.1
As-cast	24.7 ± 0.1	25.4 ± 0.1	24.9 ± 0.1	25.0 ± 0.1

observed by XLPAs is also confirmed by the HRTEM images in Fig. 9 taken at the periphery of the disks LS1 and LS2 after 10 turns of HPT. The twin lamella thickness varies between 1 and 7 nm which is in coincidence with the average twin fault spacing calculated from the twin fault probability determined by XLPAs. Namely, at the edge of the HPT disks processed for 10 turns the saturation twin fault probability value was found to be about 3 % which corresponds to an average twin fault spacing of ~ 7 nm calculated as $100 \cdot d_{111} / \beta$, where d_{111} is the spacing between the $\{111\}$ planes and β is the twin fault probability [83]. It is important to highlight that the TEM images were obtained from orders of magnitude smaller volume than the region probed by XLPAs; therefore, the statistics of the microstructural parameters determined by XLPAs are much more accurate than the ones obtained by TEM/HRTEM, and a slight deviation between the average twin fault spacing values obtained by the two methods can be acceptable.

Fig. 10 shows the XRD pole Fig. s obtained after 10 turns of HPT for the as-built LS1 and LS2 samples. It is evident that during HPT deformation the $\langle 110 \rangle$ texture in the AM-processed specimens changed to a $\langle 111 \rangle$ fiber texture.

The density measurements with a pycnometer revealed that the AM-processed specimens had a porosity of 2.5 ± 0.3 % irrespective of the applied laser scan speed, and the pore volume fraction decreased to 1.8 ± 0.2 % after 10 turns of HPT. In theory, HPT-processing may either increase or decrease the porosity. In the former case, the very high plastic strain imposed by HPT produces a large amount of vacancies and their annihilation is hindered by the applied large hydrostatic pressure. Therefore, a very high vacancy concentration is formed during HPT-processing [70]. A fraction of these vacancies annihilates when the

pressure is released after completing HPT [84]. On the other hand, the remaining excess vacancies may agglomerate and form pores. It has been shown that the increase of porosity in metallic materials processed by HPT at RT is less than 0.1 vol% [85]. For AM-processed samples, the large strain and the hydrostatic pressure applied during HPT may cause the opposite effect, i.e., the close of the pores formed during 3D printing [86]. For instance, in 316 L stainless steel processed by laser powder bed fusion, the initial porosity of the 3D-printed samples decreased by one order of magnitude from about 0.6 vol% to 0.06 vol% even after $\frac{1}{4}$ turn of HPT [86]. In the present case, such a large change in the porosity was not observed. Nevertheless, the reduction of the porosity during 10 turns of HPT suggests that the close of the pre-existing pores overwhelmed the pore formation due to the agglomeration of excess vacancies during HPT-processing of the 3D-printed CoCrFeNi MPEA samples.

3.3. Hardness evolution in the HPT-processed disks

Fig. 11 illustrates the variation of the hardness as a function of the distance from the disk center for the LS1 and LS2 CoCrFeNi samples after the different numbers of HPT turns. The hardness of the as-built LS1 and LS2 specimens was approximately 2760 ± 100 and 2680 ± 100 MPa, respectively, i.e., a considerable effect of the laser scan speed on the hardness was not observed. After $\frac{1}{2}$ turn, the hardness of the LS1 sample increased to ~ 3500 MPa in the center and to 4600–4900 MPa at the disk edge. Regarding the LS2 sample, the hardness in the center was about 4100 MPa, while at the periphery the value increased to 5200–5600 MPa. This suggests that at the beginning of HPT deformation, sample LS2 hardens faster than specimen LS1. Further increase of the number of HPT turns to one yielded a hardness of ~ 4700 MPa in the disk center, while at the edge the hardness values in the range of 5400–5700 MPa were observed for both LS1 and LS2 samples. Further increase of the number of HPT turns to 5 and 10 did not yield additional enhancement of the hardness, i.e., the saturation was achieved even after 1 turn. On the other hand, in the disk center the hardness increased from ~ 4700 MPa to about 5100–5400 MPa when the number of turns changed from one to five. Between 5 and 10 turns, significant evolution in the hardness was not observed for both samples LS1 and LS2.

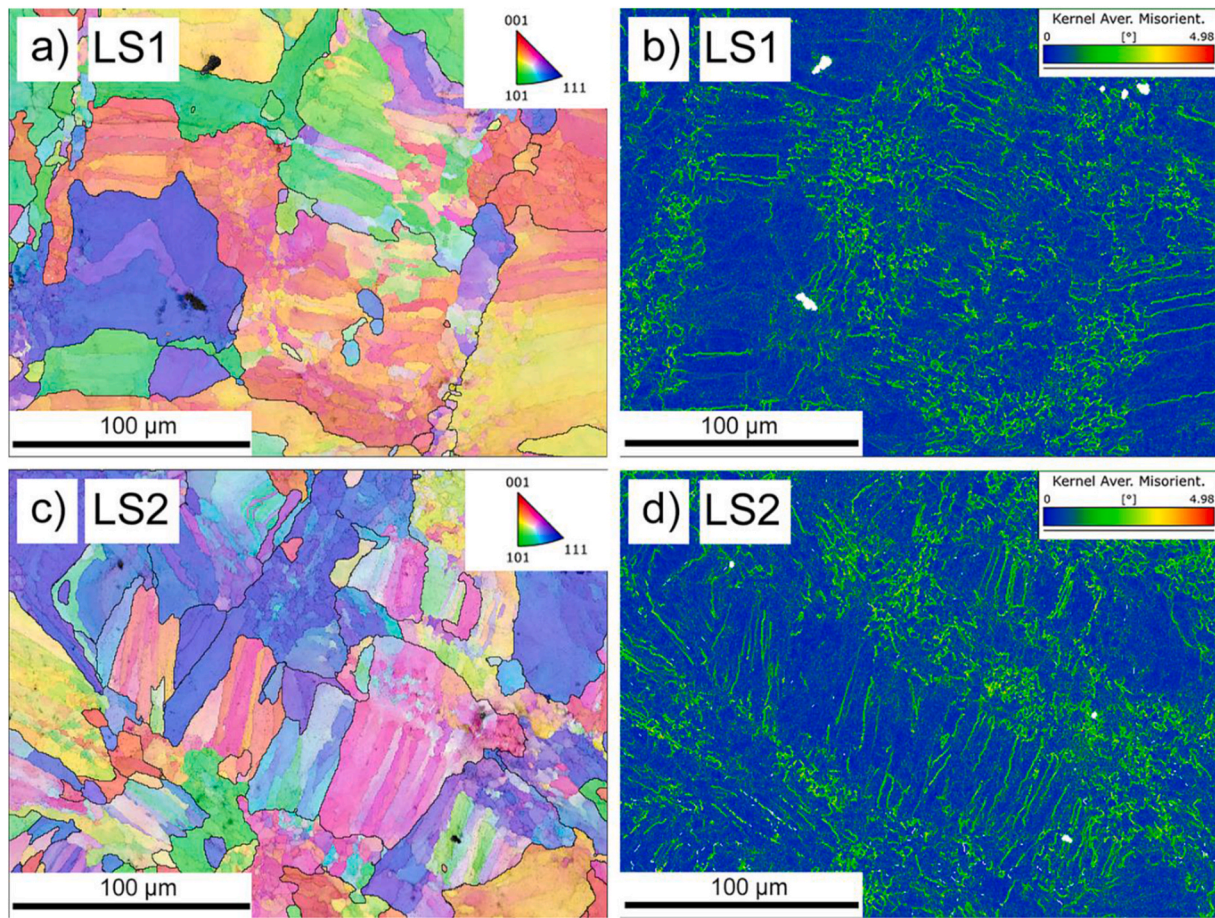


Fig. 3. EBSD images obtained on the as-built CoCrFeNi specimens, (a, b) – maps for the as-built LS1 sample, (c, d) – maps for the as-built LS2 sample, (a, c) – IPF maps, (b, d) – KAM maps.

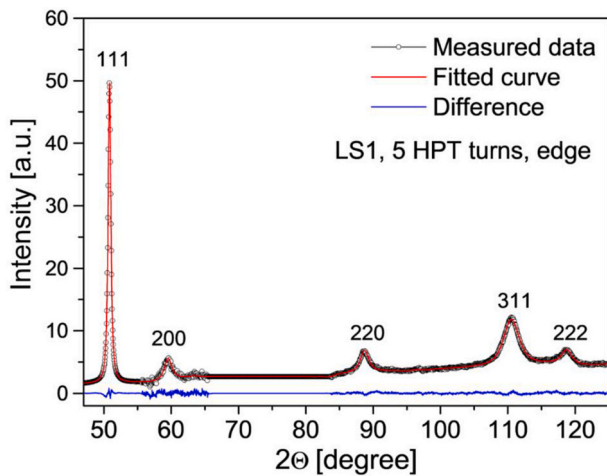


Fig. 4. CMWP fitting on the XRD pattern taken at the edge of the disk processed by HPT for 5 turns. The open circles and the red solid line represent the measured and the fitted XRD patterns, respectively, while the blue line at the bottom of the Fig. indicates the difference between them.

The benefit of utilizing the Vickers microhardness tests is the realization of the hardness inhomogeneity within a sample when the straining by HPT is not high enough, such as $\frac{1}{2}$ and 1 turn. Each indentation location indicates a different amount of shear strain introduced by HPT, which enables the relationship between hardness evolution and the introduced shear strain by HPT in the AM-processed

CoCrFeNi samples. Accordingly, Fig. 12 shows the hardness as a function of nominal shear strain for samples LS1 and LS2 processed by different numbers of HPT turns. A significant increase in hardness was observed up to the shear strain of about 25 and 12 for the specimens LS1 and LS2, and then the hardness saturated on the level of ~ 5700 MPa for both laser scan speeds. The slower increase of hardness for sample LS1 is in accordance with the slightly lower dislocation density and twin fault probability in this specimen compared to material LS2 at the same strains. It should be noted, however, that the saturation of the hardness occurred at lower shear strain values (~ 25 and ~ 12 for the specimens LS1 and LS2) than the saturation of the twin fault probability (~ 40 and ~ 20 for the samples LS1 and LS2), although twin faults are effective obstacles against dislocation glide. This apparent contradiction can be understood if we take into account that hardness testing causes an additional deformation with the equivalent strain of about 8% [87]. This value corresponds to the shear strain of $\sim 14\%$ which can explain the difference between the shear strain limits of the saturation of hardness and twin fault probability.

4. Discussion

XLPA method indicated a significant dislocation density of about $3 \times 10^{14} \text{ m}^{-2}$ in both as-built CoCrFeNi alloy samples, irrespective of the laser scan speed. These grown-in dislocations formed during AM processing in order to reduce the mismatch stresses between the grains developed under the laser beam. In addition, the local misfit stresses caused by the large temperature gradients developed during laser scanning (it can be as high as $10^\circ\text{C}/\mu\text{m}$) might also yield the formation of dislocations [56]. These grown-in dislocations may cause

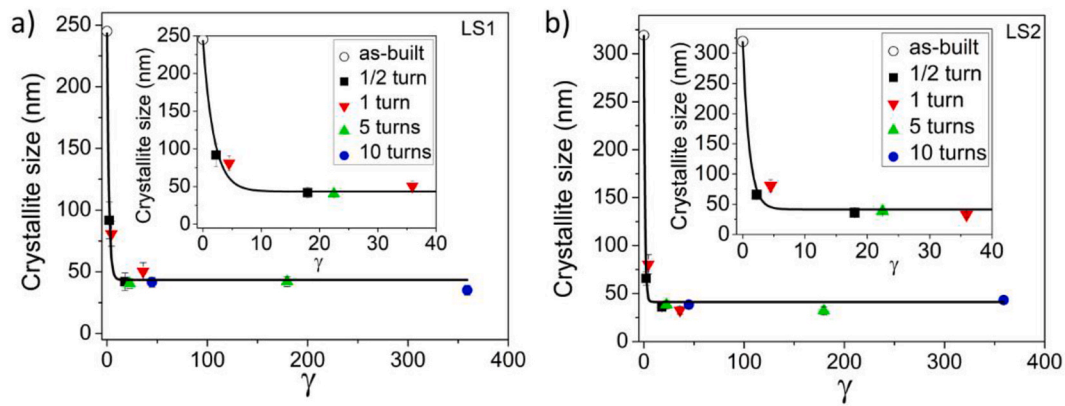


Fig. 5. Evolution of the crystallite size as a function of the nominal shear strain for samples LS1 (a) and LS2 (b). The data obtained in the centers and the edges of the disks processed for different numbers of turns are indicated by various symbols. The insets show the evolution of the microstructural parameters for low strain values.

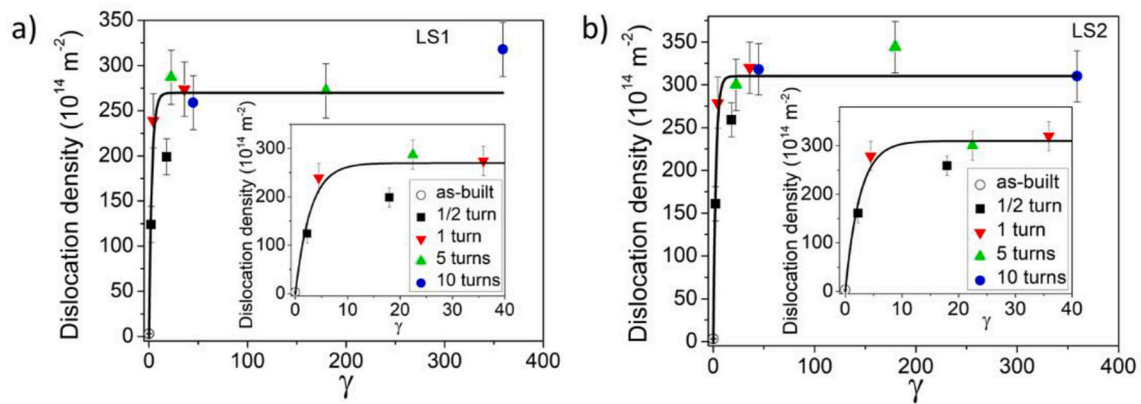


Fig. 6. Evolution of the dislocation density as a function of the nominal shear strain for samples LS1 (a) and LS2 (b). The data obtained in the centers and the edges of the disks processed for different numbers of turns are indicated by various symbols. The insets show the evolution of the microstructural parameters for low strain values.

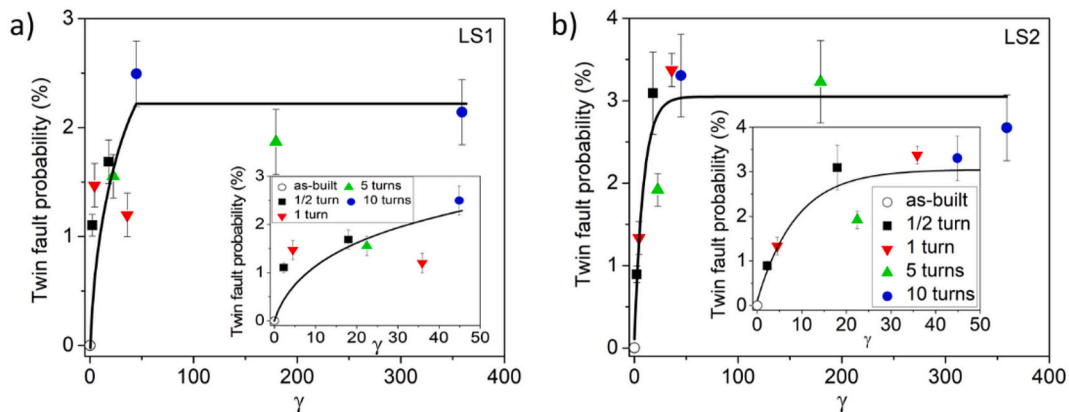


Fig. 7. Evolution of the twin fault probability as a function of the nominal shear strain for samples LS1 (a) and LS2 (b). The data obtained in the centers and the edges of the disks processed for different numbers of turns are indicated by various symbols. The insets show the evolution of the microstructural parameters for low strain values.

fragmentation of the grains if they are arranged into dense configurations (e.g., low angle grain boundaries). Indeed, Fig. 3 indicates that in the as-built samples the grains are fragmented into subgrains and in the subgrain boundaries there is a considerable lattice distortion as suggested by the high KAM values. These regions with high KAM may contain a high density of dislocations. If we inspect an as-cast CoCrFeNi alloy by EBSD, only low KAM values are detected as shown in Fig. 13.

Considerable KAM was observed only at the scratches formed due to mechanical polishing and the pits developed during additional electro-polishing (compare the KAM and image quality maps shown in Fig. 13b and c, respectively). In accordance with the low KAM values, in the as-cast CoCrFeNi sample the dislocation density was below the detection limit of XPLA (about 10^{13} m^{-2}) [74], i.e., in the AM-processed specimens the dislocation density was at least one order of magnitude larger

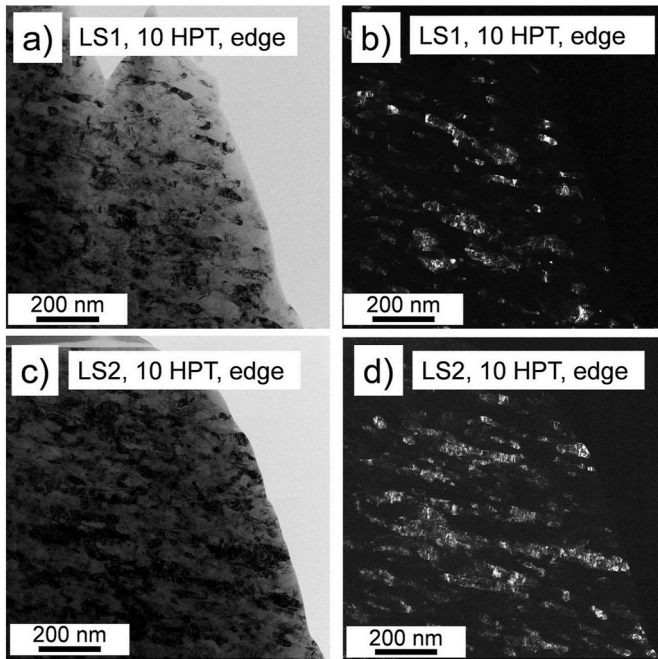


Fig. 8. Bright- (a, c) and dark-field (b, d) TEM images obtained on the edges of LS1 and LS2 CoCrFeNi disks processed for 10 turns.

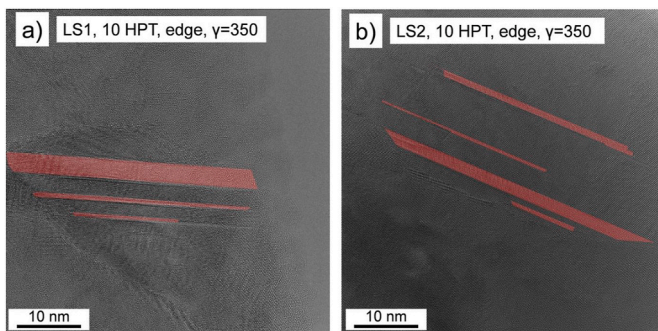


Fig. 9. HRTEM images showing twins at the edge of the LS1 and LS2 CoCrFeNi disks processed by 10 turns of HPT.

than in the as-cast counterpart. On the other hand, the grain size was similar in the as-cast and 3D-printed samples (about 90 μm). It should be noted, however, that the grains in the as-cast CoCrFeNi alloy were not fragmented into subgrains in accordance with the low KAM values; only some thick twin lamellas can be seen inside the grains in Fig. 13a. Due to the much lower dislocation density, the hardness of the as-cast specimen (1380 ± 100 MPa) was much smaller than that for the 3D-printed CoCrFeNi alloys (2700–2800 MPa). The microstructural parameters and the hardness of the AM-processed LS1 and LS2 samples and the as-cast counterpart [74] are compared in Fig. 14. It should be emphasized that the difference in the microstructure and hardness of the as-cast and 3D-printed specimens can be attributed only to the different processing routes since the chemical compositions of the two CoCrFeNi alloys were practically the same as shown in Table 1. Only the Cr content was slightly (with 1 at.%) lower in the AM-processed samples as compared to the as-cast counterpart.

Figs. 6 and 7 revealed that the laser scan speed has only a slight effect on the evolution of the microstructure during HPT-processing of the AM-processed CoCrFeNi alloy. Namely, the quantities describing the defect densities (dislocation density and twin fault probability) increased at a lower rate at the beginning of HPT deformation (at strains smaller than ~ 20) for sample LS1 than for specimen LS2. This difference can be

attributed to the different crystallographic textures in the two samples. For disk LS1, a strong $\langle 110 \rangle$ fiber texture was detected which means that the $\langle 110 \rangle$ direction was perpendicular to the HPT disk surface. Therefore, two $\{111\}$ dislocation glide planes from the four ones were lying perpendicular to the shear direction during HPT; therefore, the Schmid factors of the slip systems related to these two planes were practically zero, i.e., dislocation glide occurred only in the other two $\{111\}$ planes at the beginning of HPT. On the other hand, for sample LS2 such a strong texture was not observed, thus the slip systems in all four $\{111\}$ planes were activated. As a result, the increase of the dislocation density was faster in sample LS2 for low strains. Since deformation twinning usually occurs at the obstacles against dislocation glide (e.g., at the Lomer-Cottrell locks formed at the intersections of the $\{111\}$ slip planes), the activation of more slip systems in specimen LS2 could result in a faster increase of the twin fault probability at low strains. The effect of the $\langle 110 \rangle$ texture on the microstructure evolution in 316 L austenitic stainless steel during HPT was also discussed in Ref. [87]. In the course of HPT, in both types of samples the texture changed to $\langle 111 \rangle$, i.e., the texture effect diminished and only a very slight difference in the saturation values of the microstructural parameters was observed.

HPT-processing of both as-built CoCrFeNi MPEA samples yielded a saturation of the crystallite size and the dislocation density with values of about 40 nm and $(270\text{--}300) \times 10^{14} \text{ m}^{-2}$, respectively. Similar values were achieved for different MPEAs when HPT-processing was performed on as-cast samples [67], i.e., a pronounced effect of 3D-printing on the saturation microstructure achieved by HPT at RT was not observed. It seems that the very strong deformation during HPT blurs the differences in the initial microstructures obtained by essentially different processing methods such as casting and AM. The considerable twinning observed in the present AM-processed CoCrFeNi samples was caused mainly by the low stacking fault energy (SFE) of this composition ($20\text{--}30 \text{ mJ/m}^2$ [88]). It should be noted that the HPT-induced saturation value of the twin fault probability observed for the present 3D-printed CoCrFeNi alloy (3%) was similar to the values obtained for different HPT-processed as-cast MPEAs with low SFEs [67]. It is also worth noting that 3D-printed conventional fcc materials can have similarly high defect densities as observed in MPEA compositions. Namely, recently published studies revealed that in a conventional AM-processed fcc 316 L stainless steel the dislocation density and the twin fault probability were similar or even higher than those obtained for the present CoCrFeNi MPEA either before or after HPT [87,89]. In this effect, the similarly low SFE value (about 20 mJ/m^2) of the two alloys has a significant role, since SFE strongly influences the degree of dislocation dissociation into partials and the probability of deformation twinning, which determines the maximum dislocation density and twin fault probability achievable during HPT [70]. As a result of the comparable microstructural parameters, the hardness values of the fcc CoCrFeNi and the 316 L steel samples were very close both before (2500–3000 MPa) and after (5700–6000 MPa) HPT [87,89]. Due to this similarity in the microstructure and hardness, CoCrFeNi MPEA can be an alternative to commercial 316 L steel among the AM-processed materials.

5. Conclusions

Experiments were conducted on CoCrFeNi alloy samples manufactured by AM in order to reveal the microstructure evolution during nanostructuring due to SPD. SPD was carried out by HPT at RT up to 10 turns on two different materials 3D-printed at the laser scan speeds of 500 and 700 mm/s (denoted as LS1 and LS2, respectively). The evolution of the defect densities and the crystallite size as well as the hardness were monitored as a function of the imposed shear strain. The following conclusions were drawn from the results:

1. AM-processing at two different laser scan speeds resulted in similar grain sizes (70–90 μm) and dislocation densities ($3 \times 10^{14} \text{ m}^{-2}$). On the other hand, the texture was significantly different: for the lower

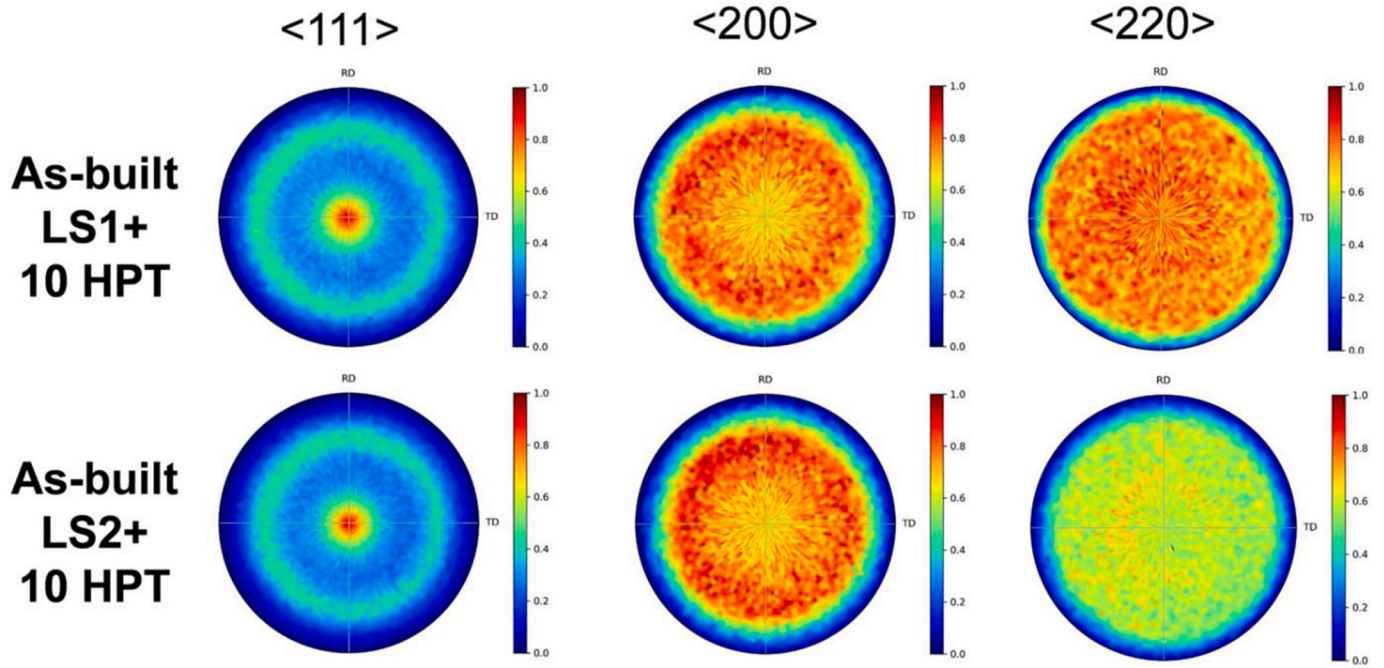


Fig. 10. $\langle 111 \rangle$, $\langle 200 \rangle$ and $\langle 220 \rangle$ XRD pole Fig. s obtained after 10 turns of HPT for the as-built CoCrFeNi LS1 and LS2 samples. The intensity in all pole Fig. s varies between zero and one due to normalization of the X-ray signal.

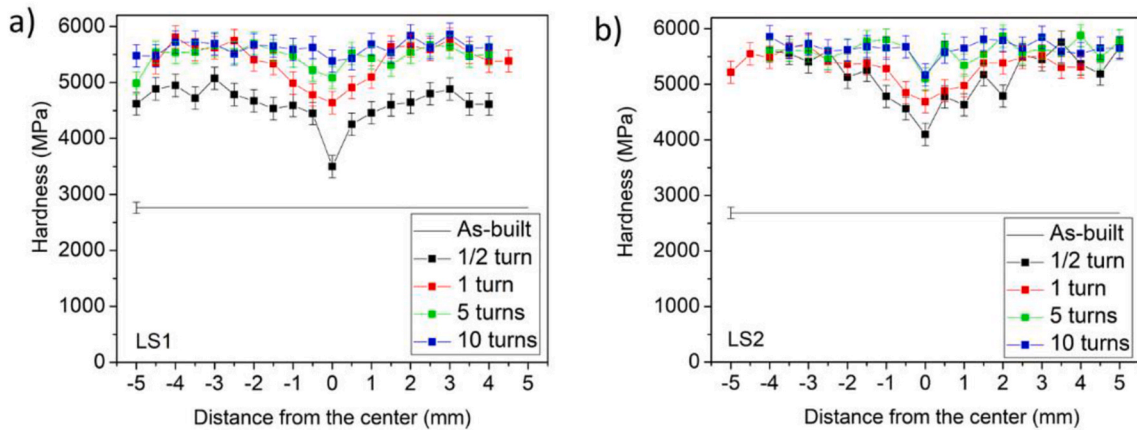


Fig. 11. The hardness versus the distance from the disk center processed by different numbers of HPT turns, a) – for LS1, b) – for LS2 disks.

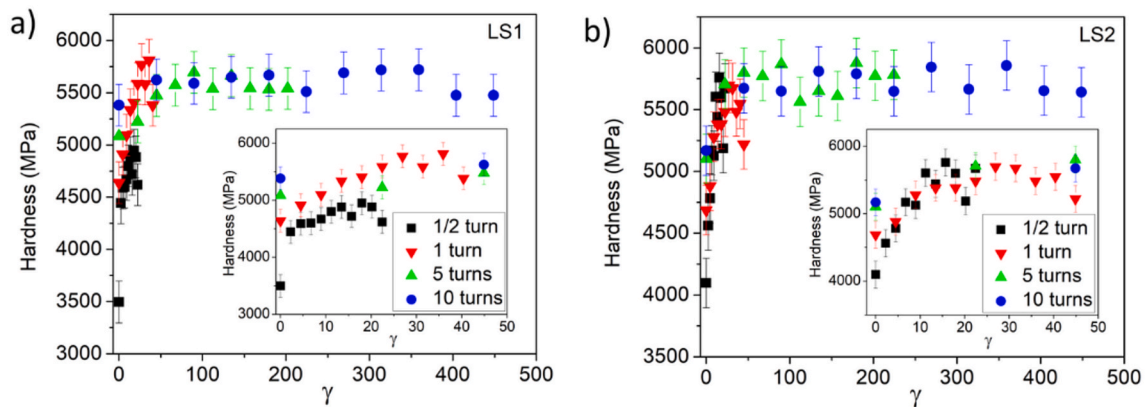


Fig. 12. Evolution of the hardness as a function of the nominal shear strain for samples LS1 (a) and LS2 (b). The data obtained in the centers and the edges of the disks processed for different numbers of turns are indicated by various symbols. The insets show the evolution of the hardness for low strain values.

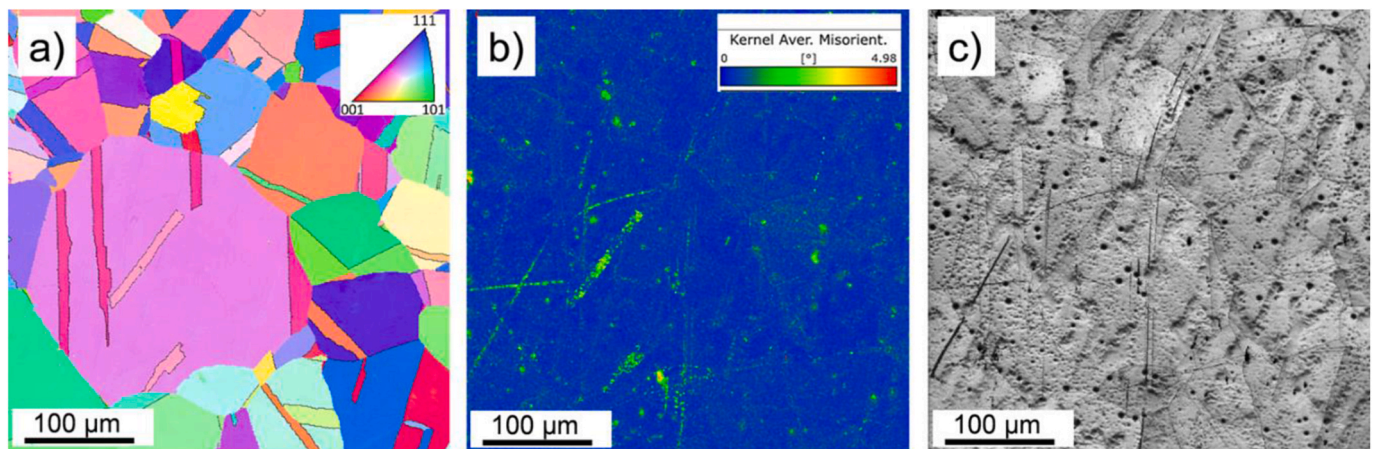


Fig. 13. IPF (a), KAM (b) and image quality (c) maps for an as-cast CoCrFeNi alloy. In the IPF map, the twin boundaries are indicated by black lines.

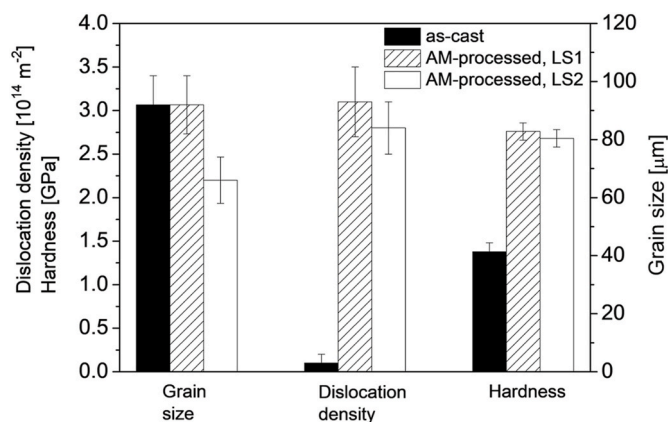


Fig. 14. The grain size, the dislocation density and the hardness for the AM-processed and the as-cast CoCrFeNi alloys [74] before HPT deformation.

laser speed a sharp $\langle 110 \rangle$ fiber texture developed which was less pronounced for the higher laser scan speeds. The considerable dislocation density is most probably formed due to the mismatch stresses between the grains developed under the laser beam and the thermal stresses caused by the large temperature gradients. The dislocation density in the AM-processed CoCrFeNi samples was at least two orders of magnitude higher than in the as-cast counterpart. As a result, the hardness of the 3D-printed specimens (about 2700 MPa) was much higher than that of the as-cast sample (~ 1380 MPa).

- The different textures in samples LS1 and LS2 resulted in a slight difference in the evolution of the defect densities for low strains of HPT. Namely, the increase of the dislocation density and the twin fault probability was faster in specimen LS2 due to the higher number of activated slip systems. This effect was also observed in the hardness evolution. On the other hand, with increasing the strain the texture changed to $\langle 111 \rangle$ for both laser speeds; therefore, the saturation values of the microstructural parameters and the hardness were only slightly different. The minimum crystallite size, the maximum dislocation density and twin fault probability were about 40 nm, $300 \times 10^{14} \text{ m}^{-2}$ and 2.5–3%, respectively, while the hardness saturated with the value of ~ 5700 MPa for both laser scan speeds. Simultaneously, elongated grains with the length and thickness of 50–300 and 10–50 nm, respectively, developed as revealed by TEM. The grains were fragmented into subgrains with a size very similar to the crystallite size obtained by the XPLA method.
- The very large differences in the initial microstructures of the samples manufactured by different processing routes (e.g., AM, casting

etc.) were blurred by the very strong deformation of HPT-processing, yielding similar nanostructures and hardness values in casted and 3D-printed materials after HPT.

Statement of conflicts of interest

The authors declare that there is no conflict of interest.

Data and code availability

Data will be made available on request.

Ethical approval

Not Applicable.

CRediT authorship contribution statement

Kamilla Mukhtarova: Writing – original draft, Visualization, Investigation, Formal analysis, Data curation. **Megumi Kawasaki:** Writing – review & editing, Investigation, Funding acquisition, Conceptualization. **Zoltán Dankházi:** Writing – review & editing, Investigation, Funding acquisition, Data curation. **Márk Windisch:** Writing – review & editing, Investigation, Formal analysis. **György Zoltán Radnóczy:** Writing – review & editing, Investigation, Formal analysis. **Weronika Serafimowicz:** Writing – review & editing, Investigation. **Jenő Gubicza:** Writing – original draft, Visualization, Validation, Supervision, Formal analysis, Conceptualization.

Declaration of competing interest

The authors declare that they have no known competing financial interests or personal relationships that could have appeared to influence the work reported in this paper.

Data availability

Data will be made available on request.

Acknowledgments

The authors thank Dr. Károly Havancsák at Technoorg Linda Co. Ltd. for the management of the thinning process of the TEM samples. This research was supported by the KDP-2021 Program of the Ministry of Innovation and Technology from the source of the National Research, Development and Innovation Fund. This research was also funded by the National Science Foundation of the United States under Grant No.

CCMI-2051205. The authors thank the support of VEKOP-2.3.3-15-2016-00002 of the European Structural and Investment Funds.

References

- J.-W. Yeh, S.-K. Chen, S.-J. Lin, J.-Y. Gan, T.-S. Chin, T.-T. Shun, C.-H. Tsau, S.-Y. Chang, Nanostructured high-entropy alloys with multiple principal elements: novel alloy design concepts and outcomes, *Adv. Eng. Mater.* 6 (2004) 299–303, <https://doi.org/10.1002/adem.200300567>.
- B. Cantor, I.T.H. Chang, P. Knight, A.J.B. Vincent, Microstructural development in equiatomic multicomponent alloys, *Mater. Sci. Eng.* 375–377 (2004) 213–218, <https://doi.org/10.1016/j.msea.2003.10.257>.
- Y. Zhang, T.T. Zuo, Z. Tang, M.C. Gao, K.A. Dahmen, P.K. Liaw, Z.P. Lu, Microstructures and properties of high-entropy alloys, *Prog. Mater. Sci.* 61 (2014) 1–93, <https://doi.org/10.1016/j.pmatsci.2013.10.001>.
- Z. Ni, Z. Li, R. Shen, S. Peng, H. Yan, Y. Tian, Achieving excellent strength-ductility balance in single-phase CoCrNiV multi-principal element alloy, *Materials* 16 (2023) 6530, <https://doi.org/10.3390/ma16196530>.
- Y. Lu, X. Gao, L. Jiang, Z. Chen, T. Wang, J. Jie, H. Kang, Y. Zhang, S. Guo, H. Ruan, Y. Zhao, Z. Cao, T. Li, Directly cast bulk eutectic and near-eutectic high entropy alloys with balanced strength and ductility in a wide temperature range, *Acta Mater.* 124 (2017) 143–150, <https://doi.org/10.1016/j.actamat.2016.11.016>.
- J. Liu, X. Guo, Q. Lin, Z. He, X. An, L. Li, P.K. Liaw, X. Liao, L. Yu, J. Lin, L. Xie, J. Ren, Y. Zhang, Excellent ductility and serration feature of metastable CoCrFeNi high-entropy alloy at extremely low temperatures, *Sci. China Mater.* 62 (2019) 853–863, <https://doi.org/10.1007/s40843-018-9373-y>.
- E.D. Tabachnikova, A.V. Podolskiy, M.O. Laktionova, N.A. Bereznaia, M. A. Tikhonovskiy, A.S. Tortika, Mechanical properties of the CoCrFeNiMnVx high entropy alloys in temperature range 4.2–300 K, *J. Alloys Compd.* 698 (2017) 501–509, <https://doi.org/10.1016/j.jallcom.2016.12.154>.
- M.G. Poletti, G. Fiore, F. Gili, D. Mangherini, L. Battezzati, Development of a new high entropy alloy for wear resistance: FeCoCrNiW_{0.3} and FeCoCrNiW_{0.3}, 3+5at.% of C, *Materials & Design* 115 (2017) 247–254, <https://doi.org/10.1016/j.matdes.2016.11.027>.
- M.-H. Chuang, M.-H. Tsai, W.-R. Wang, S.-J. Lin, J.-W. Yeh, Microstructure and wear behavior of AlxCo_{1.5}CrFeNi_{1.5}Ti high-entropy alloys, *Acta Mater.* 59 (2011) 6308–6317, <https://doi.org/10.1016/j.actamat.2011.06.041>.
- N. Birbilis, S. Choudhary, J.R. Scully, M.L. Taheri, A perspective on corrosion of multi-principal element alloys, *npj Mater. Degrad.* 5 (2021) 1–8, <https://doi.org/10.1038/s41529-021-00163-8>.
- J.R. Scully, S.B. Inman, A.Y. Gerard, C.D. Taylor, W. Windl, D.K. Schreiber, P. Lu, J. E. Saal, G.S. Frankel, Controlling the corrosion resistance of multi-principal element alloys, *Scripta Mater.* 188 (2020) 96–101, <https://doi.org/10.1016/j.scriptamat.2020.06.065>.
- K. Liu, M. Komarasamy, B. Gwalani, S. Shukla, R.S. Mishra, Fatigue behavior of ultrafine grained triplex Al_{0.3}CoCrFeNi high entropy alloy, *Scripta Mater.* 158 (2019) 116–120, <https://doi.org/10.1016/j.scriptamat.2018.08.048>.
- L.L. Xiao, Z.Q. Zheng, S.W. Guo, P. Huang, F. Wang, Ultra-strong nanostructured CrMnFeCoNi high entropy alloys, *Mater. Des.* 194 (2020) 108895, <https://doi.org/10.1016/j.matdes.2020.108895>.
- B.X. Cao, T. Yang, L. Fan, J.H. Luan, Z.B. Jiao, C.T. Liu, Refractory alloying additions on the thermal stability and mechanical properties of high-entropy alloys, *Mater. Sci. Eng.* 797 (2020) 140020, <https://doi.org/10.1016/j.msea.2020.140020>.
- S. Praveen, H.S. Kim, High-entropy alloys: potential candidates for high-temperature applications – an overview, *Adv. Eng. Mater.* 20 (2018) 1700645, <https://doi.org/10.1002/adem.201700645>.
- J.-W. Yeh, S.-J. Lin, Breakthrough applications of high-entropy materials, *J. Mater. Res.* 33 (2018) 3129–3137, <https://doi.org/10.1557/jmr.2018.283>.
- Z. Jia, T. Yang, L. Sun, Y. Zhao, W. Li, J. Luan, F. Lyu, L.-C. Zhang, J.J. Kruzic, J.-J. Kai, J.C. Huang, J. Lu, C.T. Liu, A novel multinary intermetallic as an active electrocatalyst for hydrogen evolution, *Adv. Mater.* 32 (2020) 2000385, <https://doi.org/10.1002/adma.202000385>.
- K. Li, W. Chen, Recent progress in high-entropy alloys for catalysts: synthesis, applications, and prospects, *Mater. Today Energy* 20 (2021) 100638, <https://doi.org/10.1016/j.mtener.2021.100638>.
- C. Liu, C. Yang, J. Liu, Y. Tang, Z. Lin, L. Li, H. Liang, W. Lu, L. Wang, Medical high-entropy alloy: outstanding mechanical properties and superb biological compatibility, *Front. Bioeng. Biotechnol.* 10 (2022), <https://www.frontiersin.org/articles/10.3389/fbioe.2022.952536>. (Accessed 16 December 2023).
- A. Rashidy Ahmady, A. Ekhilasi, A. Nouri, M. Haghbin Nazarpak, P. Gong, A. Solouk, High entropy alloy coatings for biomedical applications: a review, *Smart Materials in Manufacturing* 1 (2023) 100009, <https://doi.org/10.1016/j.smmf.2022.100009>.
- J. Joseph, T. Jarvis, X. Wu, N. Stanford, P. Hodgson, D.M. Fabijanic, Comparative study of the microstructures and mechanical properties of direct laser fabricated and arc-melted AlxCoCrFeNi high entropy alloys, *Mater. Sci. Eng.* 633 (2015) 184–193, <https://doi.org/10.1016/j.msea.2015.02.072>.
- A. Fu, B. Liu, S. Xu, J. Huang, Y. Zhang, Y. Cao, Y. Liu, Mechanical properties and microstructural evolution of a novel (FeCoNi)₈₆.93Al₆.17Ti₆.9 medium entropy alloy fabricated via powder metallurgy technique, *J. Alloys Compd.* 860 (2021) 158460, <https://doi.org/10.1016/j.jallcom.2020.158460>.
- J.M. Torralba, P. Alvarado, A. Garcia-Junceda, High-entropy alloys fabricated via powder metallurgy. A critical review, *Powder Metall.* 62 (2019) 84–114, <https://doi.org/10.1080/00325899.2019.1584454>.
- C. Nagarjuna, K. Yong Jeong, Y. Lee, S. Min Woo, S. Ig Hong, H. Seop Kim, S.-J. Hong, Strengthening the mechanical properties and wear resistance of CoCrFeMnNi high entropy alloy fabricated by powder metallurgy, *Adv. Powder Technol.* 33 (2022) 103519, <https://doi.org/10.1016/j.apt.2022.103519>.
- Y. Muniandy, M. He, M. Eizadjou, E.P. George, J.J. Kruzic, S.P. Ringer, B. Gludovatz, Compositional variations in equiatomic CrMnFeCoNi high-entropy alloys, *Mater. Char.* 180 (2021) 111437, <https://doi.org/10.1016/j.matchar.2021.111437>.
- S. Salifu, P.A. Olubambi, Effects of fabrication techniques on the mechanical properties of high entropy alloys: a review, *International Journal of Lightweight Materials and Manufacture* 7 (2024) 97–121, <https://doi.org/10.1016/j.ijlmm.2023.08.001>.
- S. Ford, M. Despeisse, Additive manufacturing and sustainability: an exploratory study of the advantages and challenges, *J. Clean. Prod.* 137 (2016) 1573–1587, <https://doi.org/10.1016/j.jclepro.2016.04.150>.
- M. Attaran, The rise of 3-D printing: the advantages of additive manufacturing over traditional manufacturing, *Bus. Horiz.* 60 (2017) 677–688, <https://doi.org/10.1016/j.bushor.2017.05.011>.
- B. Berman, 3-D printing: the new industrial revolution, *Bus. Horiz.* 55 (2012) 155–162, <https://doi.org/10.1016/j.bushor.2011.11.003>.
- Current advances in additive manufacturing, *Procedia CIRP* 88 (2020) 439–444, <https://doi.org/10.1016/j.procir.2020.05.076>.
- K.V. Wong, A. Hernandez, A review of additive manufacturing, *ISRN Mechanical Engineering* 2012 (2012) 208760, <https://doi.org/10.5402/2012/208760>.
- K.S. Prakash, T. Nancharaih, V.V.S. Rao, Additive manufacturing techniques in manufacturing – an overview, *Mater. Today: Proc.* 5 (2018) 3873–3882, <https://doi.org/10.1016/j.matpr.2017.11.642>.
- B. Bourell, J.P. Kruth, M. Leu, G. Levy, D. Rosen, A.M. Beese, A. Clare, Materials for additive manufacturing, *CIRP Annals* 66 (2017) 659–681, <https://doi.org/10.1016/j.cirp.2017.05.009>.
- R.A. Khas Shrutika Sharma, Vishal Gupta, Jaskaran Singh, Kanwaljit Singh, Additive manufacturing: materials, technologies, and applications, in: *Additive Manufacturing*, CRC Press, 2023.
- T. Pereira, J.V. Kennedy, J. Potgieter, A comparison of traditional manufacturing vs additive manufacturing, the best method for the job, *Procedia Manuf.* 30 (2019) 11–18, <https://doi.org/10.1016/j.promfg.2019.02.003>.
- A. Walter, C. Marcham, Environmental advantages in additive manufacturing, *Professional Safety/ASSP* 65 (2020) 34–38.
- A.A. Alogla, M. Baumers, C. Tuck, W. Elmadhi, The impact of additive manufacturing on the flexibility of a manufacturing supply chain, *Appl. Sci.* 11 (2021) 3707, <https://doi.org/10.3390/app11083707>.
- M. Delic, D.R. Evers, The effect of additive manufacturing adoption on supply chain flexibility and performance: an empirical analysis from the automotive industry, *Int. J. Prod. Econ.* 228 (2020) 107689, <https://doi.org/10.1016/j.ijpe.2020.107689>.
- A. Angrish, A Critical Analysis of Additive Manufacturing Technologies for Aerospace Applications, *IEEE Aerospace Conference*, 2014, pp. 1–6, <https://doi.org/10.1109/AERO.2014.6836456>, 2014.
- F. Careri, R.H.U. Khan, C. Todd, M.M. Attallah, Additive manufacturing of heat exchangers in aerospace applications: a review, *Appl. Therm. Eng.* 235 (2023) 121387, <https://doi.org/10.1016/j.applthermaleng.2023.121387>.
- B. Blakey-Milner, P. Gradl, G. Snedden, M. Brooks, J. Pitot, E. Lopez, M. Leary, F. Berto, A. du Plessis, Metal additive manufacturing in aerospace: a review, *Mater. Des.* 209 (2021) 110008, <https://doi.org/10.1016/j.matdes.2021.110008>.
- M. Salmi, Additive manufacturing processes in medical applications, *Materials* 14 (2021) 191, <https://doi.org/10.3390/ma14010191>.
- R. Velu, D.K. Jayashankar, K. Subburaj, Chapter 20 - additive processing of biopolymers for medical applications, in: J. Pou, A. Riveiro, J.P. Davim (Eds.), *Additive Manufacturing*, Elsevier, 2021, pp. 635–659, <https://doi.org/10.1016/B978-0-12-818411-0.00019-7>.
- M. Javaid, A. Haleem, Current status and applications of additive manufacturing in dentistry: a literature-based review, *Journal of Oral Biology and Craniofacial Research* 9 (2019) 179–185, <https://doi.org/10.1016/j.jobcr.2019.04.004>.
- P.C. Priarone, A.R. Catalano, L. Settineri, Additive manufacturing for the automotive industry: on the life-cycle environmental implications of material substitution and lightweighting through re-design, *Prog Addit Manuf* 8 (2023) 1229–1240, <https://doi.org/10.1007/s40964-023-00395-x>.
- A.H. Alami, A. Ghani Olabi, A. Alashkar, S. Alasad, H. Aljaghoub, H. Rezk, M. A. Abdelkareem, Additive manufacturing in the aerospace and automotive industries: recent trends and role in achieving sustainable development goals, *Ain Shams Eng. J.* 14 (2023) 102516, <https://doi.org/10.1016/j.asej.2023.102516>.
- ISO/ASTM 52900:2021(en), Additive manufacturing — General principles — Fundamentals and vocabulary, (n.d.). <https://www.iso.org/obp/ui/#iso:std:iso-astm:52900:ed-2:v1:en> (accessed December 17, 2023).
- Y. Zhang, W. Jarosinski, Y.-G. Jung, J. Zhang, 2 - additive manufacturing processes and equipment, in: J. Zhang, Y.-G. Jung (Eds.), *Additive Manufacturing*, Butterworth-Heinemann, 2018, pp. 39–51, <https://doi.org/10.1016/B978-0-12-812155-9.00002-5>.
- J.P. Oliveira, A.D. LaLonde, J. Ma, Processing parameters in laser powder bed fusion metal additive manufacturing, *Mater. Des.* 193 (2020) 108762, <https://doi.org/10.1016/j.matdes.2020.108762>.
- I. Yadroitsev, I. Yadroitsava, A. du Plessis, E. MacDonald, Fundamentals of Laser Powder Bed Fusion of Metals, in: Ma Qian (Ed.), *Additive Manufacturing Materials and Technologies Series*, Elsevier, 2021, <https://doi.org/10.1016/B978-0-12-824090-8.09001-6>. ii.

- [51] T. DebRoy, H.L. Wei, J.S. Zuback, T. Mukherjee, J.W. Elmer, J.O. Milewski, A. M. Beese, A. Wilson-Heid, A. De, W. Zhang, Additive manufacturing of metallic components – process, structure and properties, *Prog. Mater. Sci.* 92 (2018) 112–224, <https://doi.org/10.1016/j.pmatsci.2017.10.001>.
- [52] V. Salarvand, H. Sohrabpoor, M.A. Mohammadi, M. Nazari, R. Raghavendra, A. Mostafaei, D. Brabazon, Microstructure and corrosion evaluation of as-built and heat-treated 316L stainless steel manufactured by laser powder bed fusion, *J. Mater. Res. Technol.* 18 (2022) 4104–4113, <https://doi.org/10.1016/j.jmrt.2022.03.156>.
- [53] K.S. Mukhtarova, R.V. Shakhov, V.V. Smirnov, S.K. Mukhtarov, Microstructure and microhardness studies of Inconel 718, manufactured by selective laser melting and subjected to severe plastic deformation and annealing, *IOP Conf. Ser. Mater. Sci. Eng.* 672 (2019) 012049, <https://doi.org/10.1088/1757-899X/672/1/012049>.
- [54] T. Raza, J. Andersson, L.-E. Svensson, Microstructure of selective laser melted alloy 718 in as-manufactured and post heat treated condition, *Procedia Manuf.* 25 (2018) 450–458, <https://doi.org/10.1016/j.promfg.2018.06.100>.
- [55] L. Thijs, F. Verhaeghe, T. Craeghs, J.V. Humbeeck, J.-P. Kruth, A study of the microstructural evolution during selective laser melting of Ti–6Al–4V, *Acta Mater.* 58 (2010) 3303–3312, <https://doi.org/10.1016/j.actamat.2010.02.004>.
- [56] G. Wang, H. Ouyang, C. Fan, Q. Guo, Z. Li, W. Yan, Z. Li, The origin of high-density dislocations in additively manufactured metals, *Materials Research Letters* 8 (2020) 283–290, <https://doi.org/10.1080/21663831.2020.1751739>.
- [57] Z. Liu, D. Zhao, P. Wang, M. Yan, C. Yang, Z. Chen, J. Lu, Z. Lu, Additive manufacturing of metals: microstructure evolution and multistage control, *J. Mater. Sci. Technol.* 100 (2022) 224–236, <https://doi.org/10.1016/j.jmst.2021.06.011>.
- [58] F. Sun, T. Ogawa, Y. Adachi, K. Sato, S. Takagi, G. Miyamoto, A. Suzuki, A. Yamanaka, N. Nakada, T. Ishimoto, T. Nakano, Y. Koizumi, Modulated structure formation in dislocation cells in 316L stainless steel fabricated by laser powder bed fusion, *Mater. Trans.* 64 (2023) 1143–1149, <https://doi.org/10.2320/matertrans.MT-ME2022004>.
- [59] S. Suwas, R.J. Vikram, Texture evolution in metallic materials during additive manufacturing: a review, *Trans Indian Natl. Acad. Eng.* 6 (2021) 991–1003, <https://doi.org/10.1007/s41403-021-00271-6>.
- [60] O. Gokcekaya, T. Ishimoto, S. Hibino, J. Yasutomi, T. Narushima, T. Nakano, Unique crystallographic texture formation in Inconel 718 by laser powder bed fusion and its effect on mechanical anisotropy, *Acta Mater.* 212 (2021) 116876, <https://doi.org/10.1016/j.actamat.2021.116876>.
- [61] T. Ishimoto, S. Wu, Y. Ito, S.-H. Sun, H. Amano, T. Nakano, Crystallographic orientation control of 316L austenitic stainless steel via selective laser melting, *ISIJ Int.* 60 (2020) 1758–1764, <https://doi.org/10.2355/isijinternational.ISIJINT-2019-744>.
- [62] I. Kunce, M. Polanski, J. Bystrzycki, Structure and hydrogen storage properties of a high entropy ZrTiVCrFeNi alloy synthesized using Laser Engineered Net Shaping (LENS), *Int. J. Hydrogen Energy* 38 (2013) 12180–12189, <https://doi.org/10.1016/j.ijhydene.2013.05.071>.
- [63] Y. Brif, M. Thomas, I. Todd, The use of high-entropy alloys in additive manufacturing, *Scripta Mater.* 99 (2015) 93–96, <https://doi.org/10.1016/j.scriptamat.2014.11.037>.
- [64] B. Yuan, C. Li, Y. Dong, Y. Yang, P. Zhang, Z. Zhang, Selective laser melting of the Al_{0.3}CoCrFeNiCu high-entropy alloy: processing parameters, microstructure and mechanical properties, *Mater. Des.* 220 (2022) 110847, <https://doi.org/10.1016/j.matdes.2022.110847>.
- [65] Y. Zhao, K.B. Lau, W.H. Teh, J.J. Lee, F. Wei, M. Lin, P. Wang, C.C. Tan, U. Ramamurty, Compositionally graded CoCrFeNi_x high-entropy alloys manufactured by laser powder bed fusion: a combinatorial assessment, <https://doi.org/10.1016/j.jallcom.2021.160825>, 2021.
- [66] Z. Wu, M. He, H. Cao, S. Wang, R. Chen, B. Cao, R. Shi, X. Liu, S. Yu, S. Wang, J. Bai, J. Wei, Ultrahigh-strength and ductile CoCrFeNi-based high-entropy alloys manufactured by laser powder bed fusion with multiple strengthening mechanisms, *J. Mater. Res. Technol.* 25 (2023) 2948–2960, <https://doi.org/10.1016/j.jmrt.2023.06.110>.
- [67] J. Gubicza, Combinatorial Design of Novel Multiprincipal Element Alloys Using Experimental Techniques, *Advanced Engineering Materials* n/a (n.d.) 2301673, <https://doi.org/10.1002/adem.202301673>.
- [68] J. Gubicza, P.T. Hung, Nanostructuring of multi-principal element alloys by severe plastic deformation: from fundamentals to an improved functionality, *Mater. Trans.* 64 (2023) 1284–1298, <https://doi.org/10.2320/matertrans.MT-MF2022013>.
- [69] B. Baretzky, M.D. Baró, G.P. Grabovetskaya, J. Gubicza, M.B. Ivanov, Y.R. Kolobov, T.G. Langdon, J. Lendvai, A.G. Lipnitskii, A.A. Mazilkin, A.A. Nazarov, J. Nogués, I. A. Ovidko, S.G. Protasova, G.I. Raab, Á. Révész, N.V. Skiba, M.J. Starink, B. B. Straumal, S. Suriñach, T. Ungár, A.P. Zhilyaev, *Fundamentals of interface phenomena in advanced bulk nanoscale materials*, *Rev. Adv. Mater. Sci.* 9 (2005) 45–108.
- [70] J. Gubicza, *Defect Structure and Properties of Nanomaterials, 2nd and Extended Edition*, Woodhead Publishing, Duxford, UK, 2017.
- [71] K. Edalati, Z. Horita, High-pressure torsion of pure metals: influence of atomic bond parameters and stacking fault energy on grain size and correlation with hardness, *Acta Mater.* 59 (2011) 6831–6836, <https://doi.org/10.1016/j.actamat.2011.07.046>.
- [72] K. Edalati, Metallurgical alchemy by ultra-severe plastic deformation via high-pressure torsion process, *Mater. Trans.* 60 (2019) 1221–1229, <https://doi.org/10.2320/matertrans.MF201914>.
- [73] G. Faraji, H.S. Kim, H.T. Kashi, *Severe Plastic Deformation: Methods, Processing and Properties*, Elsevier, 2018.
- [74] J. Gubicza, P.T. Hung, M. Kawasaki, J.-K. Han, Y. Zhao, Y. Xue, J.L. Lábár, Influence of severe plastic deformation on the microstructure and hardness of a CoCrFeNi high-entropy alloy: a comparison with CoCrFeNiMn, *Mater. Char.* 154 (2019) 304–314, <https://doi.org/10.1016/j.matchar.2019.06.015>.
- [75] B. Schuh, F. Mendez-Martin, B. Völker, E.P. George, H. Clemens, R. Pippan, A. Hohenwarter, Mechanical properties, microstructure and thermal stability of a nanocrystalline CoCrFeMnNi high-entropy alloy after severe plastic deformation, *Acta Mater.* 96 (2015) 258–268, <https://doi.org/10.1016/j.actamat.2015.06.025>.
- [76] H. Shahmir, M. Nili-Ahmadabadi, A. Shafiee, M. Andrzejczuk, M. Lewandowska, T. G. Langdon, Effect of Ti on phase stability and strengthening mechanisms of a nanocrystalline CoCrFeMnNi high-entropy alloy, *Mater. Sci. Eng.* 725 (2018) 196–206, <https://doi.org/10.1016/j.msea.2018.04.014>.
- [77] J. Jang, K.-D. Liss, M. Kawasaki, X.Z. Liao, T.G. Langdon, P.Q. Dai, Hardening of an Al_{0.3}CoCrFeNi high entropy alloy via high-pressure torsion and thermal annealing, *Mater. Lett.* 151 (2015) 126–129, <https://doi.org/10.1016/j.matlet.2015.03.066>.
- [78] H. Shahmir, M.S. Mehranpour, S.A.A. Shams, T.G. Langdon, Twenty years of the CoCrFeNiMn high-entropy alloy: achieving exceptional mechanical properties through microstructure engineering, *J. Mater. Res. Technol.* 23 (2023) 3362–3423, <https://doi.org/10.1016/j.jmrt.2023.01.181>.
- [79] W. Zhao, J.-K. Han, Y.O. Kuzminova, S.A. Evlashin, A.P. Zhilyaev, A.M. Pesin, J. Jang, K.-D. Liss, M. Kawasaki, Significance of grain refinement on micro-mechanical properties and structures of additively-manufactured CoCrFeNi high-entropy alloy, *Mater. Sci. Eng.* 807 (2021) 140898, <https://doi.org/10.1016/j.msea.2021.140898>.
- [80] R.B. Figueiredo, P.R. Cetlin, T.G. Langdon, Using finite element modeling to examine the flow processes in quasi-constrained high-pressure torsion, *Mater. Sci. Eng.* 528 (2011) 8198–8204, <https://doi.org/10.1016/j.msea.2011.07.040>.
- [81] J.B. Nelson, D.P. Riley, An experimental investigation of extrapolation methods in the derivation of accurate unit-cell dimensions of crystals, *Proc. Phys. Soc.* 57 (1945) 160, <https://doi.org/10.1088/0959-5309/57/3/302>.
- [82] G. Ribárik, J. Gubicza, T. Ungár, Correlation between strength and microstructure of ball-milled Al–Mg alloys determined by X-ray diffraction, *Mater. Sci. Eng.* 387–389 (2004) 343–347, <https://doi.org/10.1016/j.msea.2004.01.089>.
- [83] J. Gubicza, X-Ray Line Profile Analysis in Materials Science, IGI Global, 1AD, <https://www.igi-global.com/gateway/book/94910> (accessed January 24, 2023)..
- [84] E. Schaffer, Effects of releasing the hydrostatic pressure on the nanostructure after severe plastic deformation of Cu, *Scripta Mater.* 62 (2010) 423–426.
- [85] Y. Qi, A. Kosinov, A.R. Kilmametov, B.B. Straumal, E. Rabkin, Generation and healing of porosity in high purity copper by high-pressure torsion, *Mater. Char.* 145 (2018) 1–9.
- [86] S.M. Yusuf, Y. Chen, N.H. Musa, N. Mazlan, N.A. Nordin, N. Nazmi, S.A. Mazlan, N. Gao, Elimination of porosity in additively manufactured 316L stainless steel by high-pressure torsion, *Int. J. Adv. Des. Manuf. Technol.* 123 (2022) 1175–1187.
- [87] J. Gubicza, M. Kawasaki, Z. Dankházi, M. Windisch, M. El-Tahawy, X-ray line profile analysis study on the evolution of the microstructure in additively manufactured 316L steel during severe plastic deformation, *J. Mater. Sci.* 59 (2024) 6008–6023, <https://doi.org/10.1007/s10853-023-09030-0>.
- [88] M. Beyramali Kivy, M. Asle Zaeem, Generalized stacking fault energies, ductilities, and twinnabilities of CoCrFeNi-based face-centered cubic high entropy alloys, *Scripta Mater.* 139 (2017) 83–86, <https://doi.org/10.1016/j.scriptamat.2017.06.014>.
- [89] J. Gubicza, K. Mukhtarova, M. Kawasaki, Nanostructuring of additively manufactured 316L stainless steel using high-pressure torsion technique: an X-ray line profile analysis study, *Materials* 17 (2024) 454, <https://doi.org/10.3390/ma17020454>.